






## Neogene hyperaridity in Arabia drove the directions of mammalian dispersal between Africa and Eurasia

Madelaine Böhme <sup>1,2✉</sup>, Nikolai Spassov<sup>3</sup>, Mahmoud Reza Majidifard<sup>4</sup>, Andreas Gärtner <sup>5</sup>, Uwe Kirscher <sup>1</sup>, Michael Marks<sup>1</sup>, Christian Dietzel<sup>1</sup>, Gregor Uhlig<sup>6</sup>, Haytham El Atfy <sup>1,7</sup>, David R. Begun<sup>8</sup> & Michael Winklhofer <sup>9</sup>

The evolution of the present-day African savannah fauna has been substantially influenced by the dispersal of Eurasian ancestors into Africa. The ancestors evolved endemically, together with the autochthonous taxa, into extant Afrotropical clades during the last 5 million years. However, it is unclear why Eurasian ancestors moved into Africa. Here we use sedimentological observations and soluble salt geochemical analyses of samples from a sedimentary sequence in Western Iran to develop a 10-million-year long proxy record of Arabian climate. We identify transient periods of Arabian hyperaridity centred 8.75, 7.78, 7.50 and 6.25 million years ago, out-of-phase with Northern African aridity. We propose that this relationship promoted unidirectional mammalian dispersals into Africa. This was followed by a sustained hyperarid period between 5.6 and 3.3 million years ago which impeded dispersals and allowed African mammalian faunas to endemically diversify into present-day clades. After this, the mid-Piacenzian warmth enabled bi-directional fauna exchange between Africa and Eurasia, which continued during the Pleistocene.

<sup>1</sup> Department of Geosciences, Eberhard-Karls-University of Tübingen, Tübingen, Germany. <sup>2</sup> Senckenberg Centre for Human Evolution and Palaeoenvironment, Tübingen, Germany. <sup>3</sup> National Museum of Natural History, Bulgarian Academy of Sciences, Sofia, Bulgaria. <sup>4</sup> Research Institute for Earth Sciences, Geologic Survey of Iran, Teheran, Iran. <sup>5</sup> Senckenberg Naturhistorische Sammlungen Dresden, GeoPlasma Lab, Dresden, Germany. <sup>6</sup> Institute of Mechatronic Engineering, Technical University Dresden, Dresden, Germany. <sup>7</sup> Department of Geology, Faculty of Science, Mansoura University, Mansoura, Egypt. <sup>8</sup> Department of Anthropology, University of Toronto, Toronto, Canada. <sup>9</sup> Institute of Biology and Environmental Science, University of Oldenburg, Oldenburg, Germany. ✉email: [m.boehme@ifg.uni-tuebingen.de](mailto:m.boehme@ifg.uni-tuebingen.de)

The Old-World desert belt, especially the Saharo-Arabian portion, plays a fundamental role in the Earth system, including (1) global aerosol production, being the most significant dust source, by modifying solar radiation, cloud physical and radiative properties, and biogeochemical nutrient cycles in oceans and on land<sup>1–6</sup>, (2) global climate evolution by inducing vegetation feedbacks on albedo and hydrologic cycle<sup>7,8</sup> and modulating Indian monsoon rainfall due to dust-induced radiative forcing<sup>9,10</sup>, and (3) organismal evolution by acting as vicariant agent in speciation of plants<sup>11–14</sup> and animals<sup>15–20</sup> because deserts, especially their largely abiotic hyperarid cores, form a very effective barrier against organism dispersal.

Today, the Saharo-Arabian desert belt divides the major biogeographic units of the Afro-Eurasian landmass into the Palearctic, Indomalayan, and the Afrotropic realms (Fig. 1). These biogeographic units share organisms with a common evolutionary history evolving in relative isolation over geologic timescales, such as many well-known examples of mammalian lineages (great apes, elephants, rhinos, horses-zebras, felid cats, buffalos, etc.).

The evolution of the present day African savannah fauna has been strongly influenced by the dispersal of faunal elements

from a late Miocene Eurasian precursor, the Pikermian palaeobiome, and it has been suggested that many lineages of African savannah mammals originate from the midlatitudes<sup>21</sup>. This strong biogeographic link between Africa and Eurasia during the Miocene<sup>22–25</sup>, facilitated by the expansion of the late Miocene Old World Savannah Palaeobiome, a grassland ecosystem in Eurasia and Africa<sup>26</sup>, is biased, however, towards Eurasian immigrants into Africa<sup>22,27</sup>, which later evolved endemically, together with the autochthonous taxa, into extant Afrotropical clades during the last 5 million years<sup>24</sup>. Faunal exchange during the Plio-Pleistocene was suggested to be promoted by eustatic sea-level variations<sup>27</sup> and to be limited by North African aridification<sup>26</sup>.

We, on the contrary, argue that climatic variations of northern Arabia were critical for Africa-Eurasian mammalian interchange in the Neogene, including important aspects of human evolution, because northern Arabia (north of ~25° N, e.g., Negev, Nefud, and Syrian deserts) acts as a gateway between Africa and Eurasia (Fig. 1). To obtain a palaeoclimatic proxy record of northern Arabia, we investigated geochemically and sedimentologically a 2.6 km-thick terrestrial section spanning 10 million years of continuous stratigraphy between the middle Miocene and early

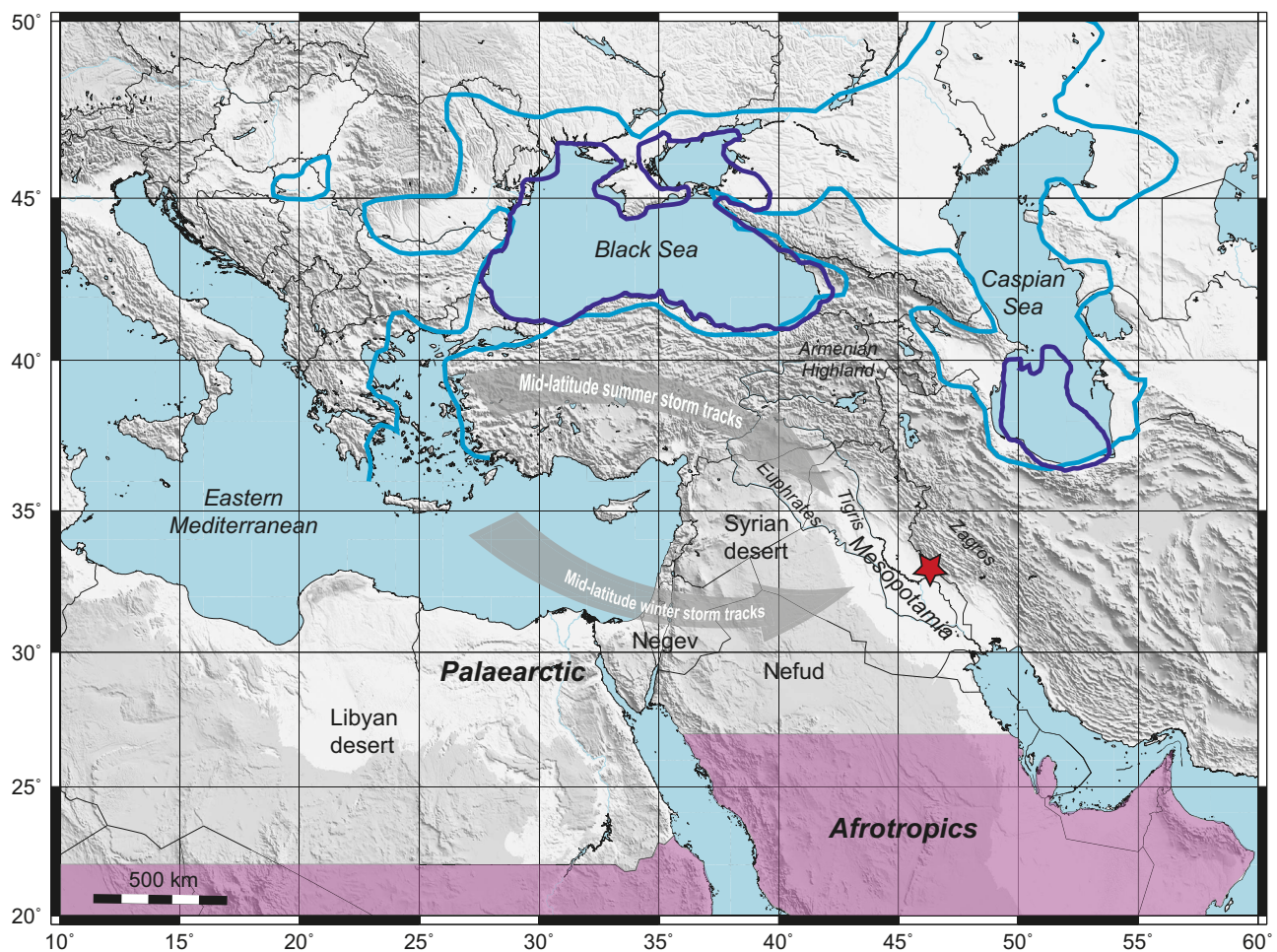


**Fig. 1 Topographic map of the Eastern Mediterranean and Western Asia.** The red star indicates the field area in the folded Zagros; about 1000 km East of the Mediterranean Sea and 570 km south-southeast of the Caspian Sea, between the Mesopotamian plain and the Zagros Mountains. Light blue line represents coastline of Paratethys during the Pontian (6 Ma) highstand, dark blue line represent coastline during Pliocene lowstand (Productive Series<sup>52,88</sup>). Highlighted are large-sized extant deserts west of Mesopotamia, the source of Euphrates and Tigris rivers in the Armenian highland north of Mesopotamia, and the principal positions of mid-latitude storm tracks during northern hemispheric summer (bringing dust) and winter (bringing rain). The present-day transition between Afrotropic (purple) and Palearctic biogeographic realms (sensu<sup>123</sup>) runs around 25° northern latitude. Topographic map is created using generic mapping tools of<sup>124</sup> and the topographic dataset ETOPO1 of<sup>125</sup>.



**Fig. 2 Gahsaran Formation.** **a** Symmetrical wave ripples (13.0 Ma). **b** Massive pedogenic gypsum (12.5 Ma). **c** Last marine bed of fossiliferous sandy limestone (12.3 Ma). **d** *Clausinella amidae* (Veneridae) from the top bed (**c**).

Pleistocene<sup>28</sup>, exposed in the present-day arid Mesopotamian Basin at the foothills of the Zagros Mountains (Fig. 1). We combine our results with genus-level analysis of mammalian dispersals collected from Eurasian and African faunas between 9 and 3 Ma. Our study reveals a sustained period of hyperaridity in the Pliocene and a number of transient hyperaridity intervals in the late Miocene, which coincide with lake-level lowstands of the Paratethys, and explain observed temporal changes in Afro-Eurasian mammal dispersals. Based on these observations, we propose a new climatically driven model for faunal dispersion between western Asia and Africa.

## Results and discussion

**Geology and sediment characteristics.** The SE-NW trending Zagros Mountain Belt originated from the collision of the Arabian and Persian plates during closure of the Neothetys<sup>29,30</sup>. It is divided into four main parts comprising 1) the Sanandaj-Sirjan metamorphic zone, 2) the Imbricated Belt, 3) the Simple Zagros Folded Belt, and 4) the Mesopotamian Foreland Basin<sup>28</sup>. The Zagros Fold Belt is comprised of more than nine kilometers of Mesozoic to Cenozoic sediments of largely marine Neotethyan origin, including a continuous 3 km-thick sequence of continental sediments of the Agha Jari and Bakhtyari Formations. The field area in the Push-e Kush arc of the Folded Zagros Belt is near the Iran-Iraq border (coordinates 33N, 46.5E). Today, it is characterised by arid climate and excellent natural exposures with ~3 km long continuous profiles from the Gahsaran, Agha Jari to Bakhtyari Fms, exposed in two easily accessible synclinal-anticlinal structures of Changuleh (Supplementary Fig. S1) and Zarrinabad. A previous magnetostatigraphic study by Homke et al.<sup>28</sup> gives robust temporal control for 2.6 km-thick sediments exposed in both structures, which are dated to between 13 and 2 Ma.

The shallow marine Gahsaran Formation (corresponding to Lower Fars Fm in Syria, Fatah Fm in Iraq, Dam Fm in Arabia) consists of thick and well-bedded evaporites, red silty clays and

green to brown sandstones. The upper part of the Gahsaran Fm is characterised by reddish muds, alternating with dm-scale carbonate and fine-sandstone beds (Fig. 2). Sandstones show frequently symmetric wave-ripples on top (Fig. 2a) with carbonates (marls) rich in marine, mud-flat type trace-fossils (fecal pellets and cf. *Dactyloides*). Red muds contain regularly pedogenic gypsum concretions, sometimes showing redox-mottling and, at profile meter 110, a 0.8 m thick gypcrete (Fig. 2b). These observations suggest fluctuating sea-levels between shallow marine (shoreface) and terrestrial (backshore) depositions. The top of Gahsaran Fm can be placed at the last marine bed, which we observe at stratigraphic meter 130. This 0.25 m thick sandy limestone contains abundant marine shells (Fig. 2c, d, *Clausinella amidae*, a Venus clam) and dates to 12.3 Ma.

The Agha Jari Fm represents a 2.4 km-thick depositional profile of fine-clastic to fluvial sediments (Fig. 3), which is widely distributed in the Mesopotamian Foreland Basin (also known as Upper Fars Fm in Syria, Injana Fm in Iraq and Dibdiba Fm in Kuwait) and dated by magnetostratigraphy in the Push-e Kush arc from the late Middle Miocene (12.3 Ma) to the base of the Pleistocene (~2.5 Ma<sup>28</sup>). It is subdivided into two members: the lower Agha Jari Member and the Lahbari Member. The basal parts of the Agha Jari Member consists of greyish to reddish silty clays with interbedded channels filled with sandstones<sup>28</sup>. Overbank sediments between 12.3–11.5 Ma show a dominance of pedogenic gypsum-bearing red muds (Fig. 3a), virtually indistinguishable from the underlying Gashraran muds, intercalated by few dm-scale fine-sandstone horizons without wave-ripples. At 11.5 Ma one of the last pedogenic gypsum concretions for the entire section occurs (Fig. 3i and Supplementary Fig. S2e) and the fine-clastic sediments show increasingly better developed palaeosol-horizons (Fig. 3b), including rubification and clay lesvage. Beginning at 11.45 Ma fluvial sandstones thicken (>5 m, thus contributing to rough surface topography) and show the first cross-bedding structures (Fig. 3c). At 10.8 Ma strongly cross-bedded sandstone bodies are >10 m thick and show substantial channel-lag clasts (mainly chert

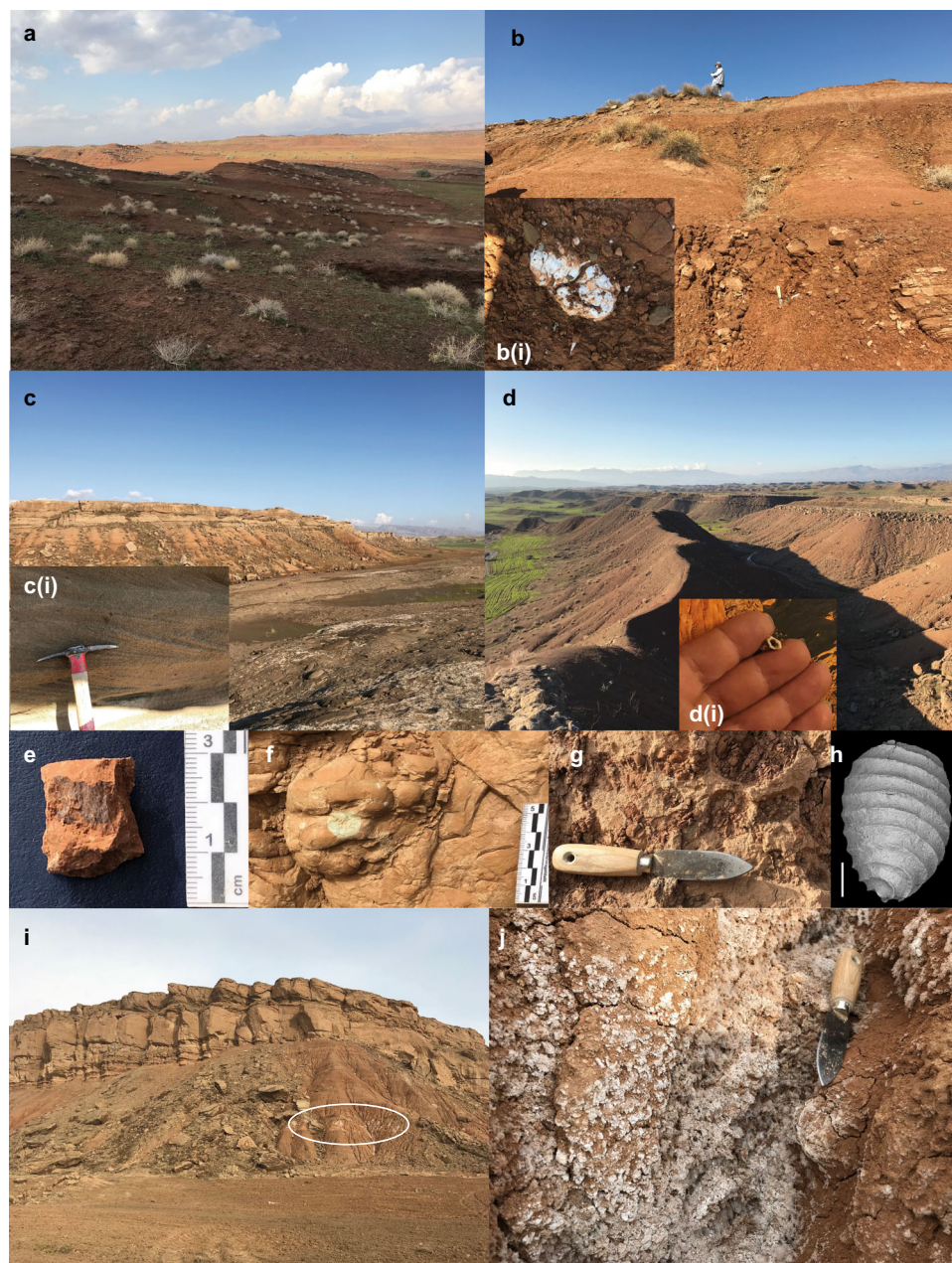


**Fig. 3 Agha Jari Formation.** **a** Base of Agha Jari Formation; red mud and dm-scale fine-sandstones (12.3–11.5 Ma). **b** Intensification of palaeosol formation and (b(i)) concretion of pedogenic gypsum (11.5 Ma). **c** Cross-bedded sandstones becoming dominant (>10 m thickness) sedimentary features (10.8 Ma). **d** Thinning sandstones and dispersed pedogenic carbonates (**d(i)**)—rhizocretes appear (9.4 Ma). **e–h** Indicators for elevated soil moisture and ephemeral floods between 8.70 and 8.55 Ma and at 8.39 Ma (**e** manganese staining of clay cutans, **f** root halos, **g** mud-ball erosion on channel-fill base, **h** charophyte gyrogonite, scale bar is 100  $\mu\text{m}$ ). **i** Most massive sandstone bodies (60 m thick) of cross-bedded medium-grained sandstones deposited between 6.15 and 5.95 Ma. Circled is the first saline soil bed (see **j**). **j** Salt efflorescence as it appeared few days after rain (6.25 Ma).

and intra-formational clasts) at their base. Palaeosols show a relatively intense reddish-green mottling at this time (Munsell dry colour: 10R 5/4, Gley1 8/5G) and common root halos. They are highly calcareous (carbonate content of all fine-clastics of the Agha Jari Formation is high, probably 20–30% according to field/HCl tests). Heavy mineral composition of sandstones shows the presence of olivine and a strong garnet-mica-amphibole signal, indicating the (palaeo-)Tigris as the main source (see Supplementary information chapter 3 and Fig. S9). This agrees with published channel orientation and palaeoflow directions towards to SE, parallel to the Mesopotamian drainage and the course of present-day Tigris river<sup>28</sup>.

At 9.7 Ma sandstone bodies thin and the first pedogenic carbonates occur as rhizocretes (Fig. 3d). The sparitic infill of these plant-root tubes suggests diagenetic overprinting. Despite the highly calcareous sediments, pedogenic carbonates were only observed as small rhizocretes and calcareous mycelium between 9.78 and 6.9 Ma. At 8.8 Ma sandstones thicken again and show cross-bedding and through-bedding structures. Fluvial channels show frequent mud-ball erosion (Fig. 3g) at their base, which are reported to be indicative of ephemeral floods in mostly semi-arid<sup>31</sup>, but also humid climates<sup>32</sup>. Between 8.75 and 7.5 Ma indicators of higher soil-moisture, such as manganese staining on clay cutans (Fig. 3e) and large and intense plant-root halos

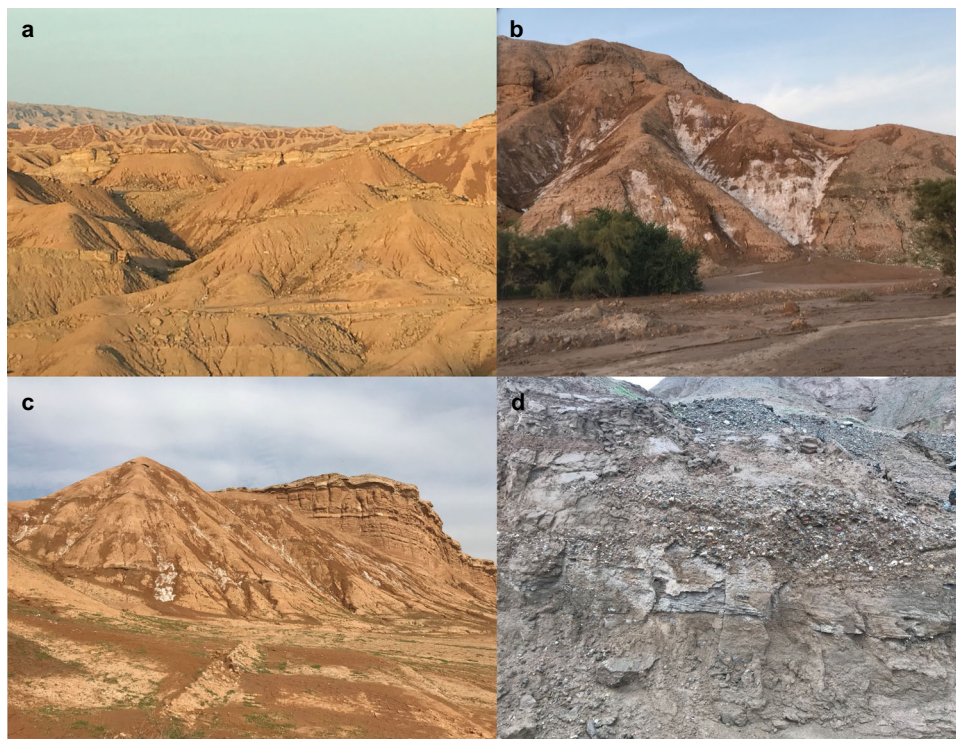


**Fig. 4 Lahbari Member.** **a** Transition of lower member Agha Jari Formation (foreground, with minor sandstone layers) to Lahbari Member (background, “pyramidal” erosional features) at 5.6 Ma. **b** After rain, massive salt efflorescence on silts (5.5–5.1 Ma). **c** Transition from mud-dominated (foreground with salt efflorescence) to very-fine sand dominated part (background) of the Lahbari Member (5.0 Ma). **d** First cobble-size conglomerates at 3.5 Ma indicate the transition to the Bakhtyari Formation starting at 2.5 Ma with boulder-sized conglomerates. The transition to Bakhtyari Formation is concordant (contra<sup>28</sup>).

(Fig. 3f) are regularly observed. Furthermore, rare finds of aquatic gastropods at 8.78 Ma and charophyte algae (Fig. 3h) at 8.69 and 8.56 Ma indicate the existence of water bodies within the alluvial plain. The extremely small size (463–580  $\mu\text{m}$ ,  $n = 7$ ) and mass occurrence of charophyte gyrogonites (10 specimens per gram of sediment), suggest that this water bodies were seasonal in nature (the absence of fluvial erosive features excludes ox-bow lakes) and may have developed after extensive rains. Mass occurrence of small-sized gyrogonites is indicative for environmental stress within temporary ponds<sup>33</sup>.

Further up-section (after 8.4 Ma) sandstone bodies decrease in thickness again and indications of elevated soil-moisture are lacking. At 6.25 Ma a 1-m thick whitish horizon is found (Fig. 3i), which turned out to be a reddish silty mud covered by needle-like salt crystals on the surface (Fig. 3j). This salt efflorescence was observed 1 week after rain (November 15/16, 2018) and disappears rapidly (according to local observers) probably due to wind erosion and hygroscopic behaviour. Macroscopic salt crystals, salt crusts or pans, halite pseudomorphs, or other signs of leaching and reprecipitations have not been observed within this (and younger salt-bearing) sediment, suggesting that the salt (mostly halite) is finely dispersed in the mud and was not leached after deposition. Directly above this saline horizon a package of the most dominant fluvial channels of the entire Agha Jari Formation appears (Fig. 3i, three sandstone bodies of 60-m total thickness), dated to between 6.15–5.95 Ma. Afterwards sandstones became rare and disappear at 5.6 Ma, marking the top of lower Member of Agha Jari Formation.

The Lahbari Member, the upper part of Agha Jari Formation, is a regionally continuous lithostratigraphic unit, developed parallel to the Zagros Mountain front over a distance of ~900 km, from the Lurestan Province in northwest Iran till the Coastal Fars

Province in southern Iran<sup>34</sup>. The Lahbari Member is characterised by structureless and uniformly beige (hue 5–10R, 2.5YR) coloured saline mud sedimentation without palaeosol development (e.g., absence of rubification, lessivation, redoximorphic features, and accumulations of carbonates, sulphates or chlorides). It shows infrequent fluvial channels (Fig. 4) of very fine sandy grainsize (in contrast to fine-to-medium sized sand in the lower Agha Jari Member), where sandstone layers are clay-rich, less consolidated and thinner than 5 m. A colour changes in aerial photographs (see Supplementary Fig. S1) is related to this suppression of fluvial sandstones. The most intriguing feature of the Lahbari Member, however, is that it is predominantly composed of saline sediments, giving their outcrops (especially during time interval 5.59–5.1 Ma) a “snow-coverage”-like appearance after a rain event (Fig. 4b, c). Stratified salt accumulations as crusts or pans are not developed. Sandstones are mostly lacking in this time period and re-appear after 5.1 Ma (Fig. 4c). At 3.5 Ma the first cobble-sized conglomerates of predominantly Mesozoic limestone clasts were observed as small-scale channels interfingering the silty to fine sandy background sediments (Fig. 4d). A further coarsening upward trend in conglomerate size is observed, but first boulder-sized objects (characterising the Bakhtyari Formation) appear concordantly and rather suddenly at the beginning of the Pleistocene (2.5 Ma), which documents the progression of the Zagros Mountain Front Flexure<sup>28,35</sup>.

**North Arabian hyperaridity.** It has been shown that the geochemistry of soluble salts in desert soils is sensitive to humidity gradients from hyperarid to semi-arid conditions<sup>36,37</sup>, with less soluble salts in wetter soils. In particular, chloride and nitrate contents in soils are excellent proxies for hyperaridity (Table 1,

**Table 1 Climatic thresholds of soluble anion concentration in Neogene Iranian sediments.**

Climate	P/PET	MAP <sup>a</sup> (mm)	Nitrate <sup>b</sup> ( $\mu\text{mol g}^{-1}$ )	Chloride <sup>b</sup> ( $\mu\text{mol g}^{-1}$ )	Cl <sup>-</sup> /Br <sup>-</sup> molar ratio
Hyper-arid	<0.05	<100	>2	>40	≥650
Arid	<0.2	100–400	0.05–2	0.2–40	≤650
Semi-arid	<0.5	400–1000	<0.05	<0.2	<125

<sup>a</sup>Based on actual PET at sampling site of 2000 mm (Flint et al.<sup>126</sup>).

<sup>b</sup>Based on data from Rosenthal et al.<sup>37</sup> and Ewing et al.<sup>36</sup>.

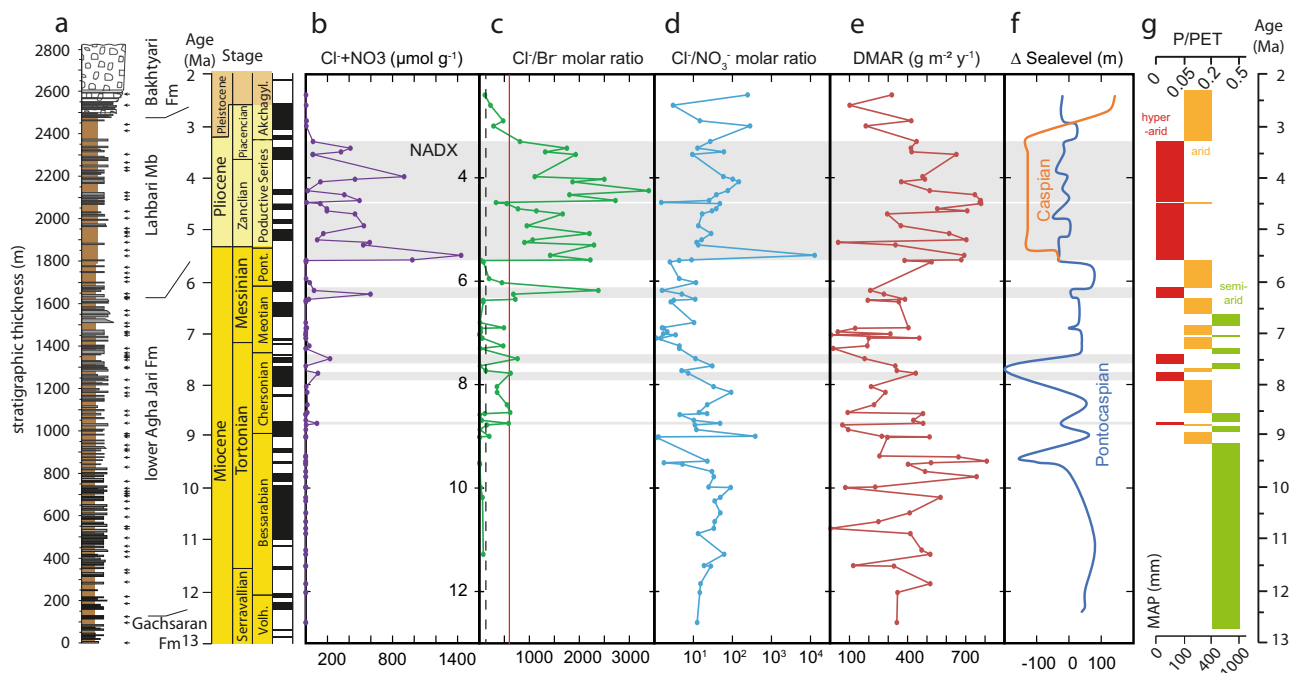


**Fig. 5 Neogene of the Zarrinabad and Changuleh syncline: chronological, geochemical, and sedimentological data.** **a** Lithology, stratigraphy<sup>28</sup>, and sampling points. **b** Chloride and nitrate concentration of silts and palaeosols (Supplementary Data 1), **c** Chloride/bromide molar ratio (dashed line represents ratio in the upper troposphere; red line is the ratio of seawater, see “Methods” section). **d** Chloride/nitrate molar ratio. This ratio does not exceed 700 in continental evaporites, but is increased by two to three orders of magnitudes in seawater and marine halite (see “Methods” section, Supplementary Fig. S4 and Supplementary Data 2). **e** Dust mass accumulation rates (DMAR) of dry deposition (for details see Supplement chapter 2). **f** Paratethyan sea-level (see “Methods” section), blue line Ponto-Caspian sea-level (Black Sea since 6 Ma), orange line Caspian sea-level. **g** Climatic interpretation according to thresholds in chloride and nitrate concentrations in solutions (see “Methods” section and Table 1; red—hyperarid, orange—arid, green—semi-arid). Climate classification is based on ratio of precipitation (P) to potential evapotranspiration (PET) and mean annual precipitation (MAP) is calculated based on actual PET at sampling site of 2000 mm. Arabian hyperarid periods are shaded in grey.

see “Methods” section for details). In the absence of leaching, both highly soluble anions accumulate in hyperarid regions ( $P/PET < 0.05$ ) from atmospheric (aeolian) wet and dry deposition<sup>38</sup>.

Our Mesopotamian proxy record (median sampling resolution 90 kyrs) reveals substantial changes in total soluble salt (TSS) content between 0.05–8.70% along the studied section (Supplementary Fig. S2). Fluctuations in anion concentrations started to become pronounced from 9 Ma onwards (Fig. 5 and Supplementary Figs. S2 and S3) and reached maximum amplitudes during the second part of the late Miocene, with overall elevated values during most of the Pliocene. Chloride and nitrate exceeded the threshold values for hyperaridity (Table 1) at 8.75 Ma (~8.76 to ~8.72 Ma), 7.78 Ma (~7.91 to ~7.75 Ma), 7.50 Ma (~7.57 to ~7.40 Ma) and 6.25 Ma (~6.30 to ~6.10 Ma) and especially between 5.59 and 3.3 Ma, with a short interruption at 4.48 Ma (Fig. 5b and Supplementary Fig. S3a, b). We interpret this salinity signals in terms of aridity rather than tectonics, because the Mesopotamian Foreland Basin was well-drained and hydrologically open during

its existence<sup>39</sup> with lithostratigraphic formations widely distributed<sup>34</sup>, excluding the development of dry playas near the Zagros front, which typically develop in the centre of tectonically closed basins<sup>40</sup>.

The highly soluble anions chloride and nitrate were significantly elevated during hyperarid periods (20–65 wt% relative to TSS; Supplementary Fig. S3d), during which no palaeosol formation was observed in the field. This is especially true for the Lahbari Member, composed of structureless beige mud, a sustained hyperarid period, which we term the Neogene Arabian Desert climaX (NADX). Palynological investigations reveal for the beginning of NADX a herbal halophytic desertic vegetation dominated by Chenopodiaceae (for details see Supplementary information chapter 4). This period is also characterised by significantly elevated dust mass accumulation rates (DMAR) reaching almost  $800 \text{ g m}^{-2} \text{ y}^{-1}$  (Fig. 5e), a reduced fluvial run-off (Supplementary Fig. S2e) and common occurrence of the mineral celestine (an aridity indicating strontium sulphate, see Supplementary information chapter 3). In contrast to sandstones from

the pre-NADX period, which show a (palaeo-)Tigris provenance, muds and fine-sands from hyperarid intervals rather resemble the (palaeo-)Euphrates and thus a more westerly source (for minerals and provenance analysis see Supplementary Fig. S10 and Supplementary information chapter 3), suggesting a change in prevailing wind-direction during NADX.

The NADX is bracketed by two prominent glacial intervals; the Messinian marine isotope stage (MIS) TG14 glacial (5.585 Ma<sup>41</sup>) and the Piacenzian MIS M2 glacial (3.295 Ma<sup>42,43</sup>), both marked by significant eustatic sea-level drops down to 60 m below present-day values<sup>44,45</sup>. The termination of the NADX at 3.3 Ma coincides with the beginning of the mid-Pliocene Warm Period (3.265–3.025 Ma<sup>46</sup>), whereas NADX initiation at 5.59 Ma is coeval with the acme of the Messinian Salinity Crisis (MSC, stage 2 or “Messinian gap”<sup>47</sup>) supposedly related to a high-amplitude Mediterranean base-level drop of  $\geq 1500$  m<sup>48–50</sup> and a low-amplitude base-level drop in the Ponto-Caspian part of the Paratethys<sup>51,52</sup>. The highest concentration of TSS (8.70%) and chloride (1432  $\mu\text{mol/g}$ ) is recorded in sample IC45 dated to  $5.50 \pm 0.05$  Ma, thus overlapping in age with the “Messinian gap” (5.59–5.53 Ma<sup>41</sup>). This sample shows an exceptionally high chloride/nitrate ratio of  $13 \times 10^3$  (Fig. 5d), unlike hyperarid desert soils (see “Methods” section), but similar to sea-water and marine halite ( $6\text{--}53 \times 10^3$ ; Supplementary Fig. S4), suggesting a marine origin of anions in this sample. During the NADX, fluvial runoff from the palaeo-Tigris river is extremely reduced, especially between 5.6 and 4.3 Ma (Fig. 4, Supplementary Fig. S2e). The highest runoff in terms of most densely stacked fluvial channels is observed immediately before the NADX, between 6.15 and 5.95 Ma (Fig. 3h and Supplementary Fig. S2e), suggesting intense rainfall in Tigris headwaters in the Armenian highlands (Fig. 1) at this time.

In contrast to NADX, the duration of Miocene hyperarid periods are relatively short ranging between 70–200 kyrs (at 6.25 Ma) and  $\sim 40$  kyrs (at 8.75 Ma). From 9.4 to 5.6 Ma DMAR are comparatively low and the amplitudes of humidity changes are maximal, containing six shorter periods of semi-arid climate conditions during which DMAR are strongly reduced. The most humid climate according to field-based soil-moisture indicators and fossils (Mn-staining, clay cutans, root halos and depletion coatings, temporary pond charophytes and snails; Fig. 3e–h) occurs between 8.70–8.55 Ma, similar to the Mediterranean<sup>53</sup>. In the older part of our record geochemical proxies and well-developed, partly rubified B-horizons of palaeosols with reddish-green mottling, root halos, clay lessivation, and rare gypsum concretions (Fig. 3b and Supplementary Fig. S2e) point to a persistent semi-arid climate lacking strong variability on longer timescales. A period of significantly elevated DMAR, decreased Tigris runoff and rhizocretion formation is observed between 9.8 and 9.4 Ma (Figs. 3d and 5e and Supplementary Fig. S2e), coinciding with a period of a reduced hydrologic cycle in Europe<sup>53</sup>. Between 7.4 and 6.8 Ma, the time of initial Sahara desertification<sup>54–56</sup>, the Mesopotamian climate is comparatively humid, switching between arid and semi-arid conditions (Fig. 5g).

**Driving forces of North Arabian deserts.** During present-day northern hemispheric summer, the Mediterranean and the Near East are under the influence of the subtropical jet stream and the associated high-pressure belt, leading to subsidence and surface divergence of stratified dry air masses. Precipitation in Mesopotamia is derived from the southward retreat of the polar front jet stream during the boreal winter, and its westerly storm-tracks originating over the Mediterranean<sup>57</sup>. Cyclonic activity and labile air masses convey rain into North Arabia. Hence, we propose that

Arabian hyperaridity could be a consequence of disruption and blocking of winter-season westerlies and cyclogenesis.

A mechanism explaining our observations is represented by the influence of the Siberian High (SH) pressure system<sup>58</sup> on Southwest Asia. The extent of the eastern Paratethys in Central Asia and within the Ponto-Caspian domain affect synoptic atmospheric pressure systems over Eurasia via seasonal change of land-sea thermal contrast<sup>59</sup>. Paratethys retreat and concomitant decrease of moisture production will enforce the SH during winter and expand its influence westward<sup>60</sup>. Clockwise motion of the SH anticyclone enforces south-easterly winds over Western Asia, thereby deflecting westerlies northward and inhibiting cyclogenesis over the eastern Mediterranean<sup>58</sup>. During boreal summer, a smaller Paratethys weakens surface pressure over West Asia<sup>60</sup>, thereby enforcing the low over the Zagros Mountains, which today is responsible for advection of strong dust-laden north-westerly wind during summer in Mesopotamia, the so-called Shamal<sup>61</sup>. In summary, modelling indicates that a Paratethys shrinkage reduces winter rain and increases summer storminess in Western Asia, particularly northern Arabia.

The history of proposed Ponto-Caspian sea-level fluctuations (see “Methods” section) matches very well our Arabian aridity and dust records, where periods of low Caspian sea-level correspond to hyperaridity, enhanced DMAR and reduced palaeo-Tigris run-off in Mesopotamia (Fig. 5e–g and Supplementary Fig. S2e). This is especially evident during the 2.3 Myr long NADX interval (5.59–3.3 Ma), which corresponds to the  $>2$  Myrs long separation of the Caspian Sea from the Black Sea Basin and hence the Mediterranean<sup>62,63</sup>. Caspian sea-level dropped by at least 200 m in two steps at 5.6 Ma (climax of MSC “stage 2”) and 5.38 Ma (Fig. 5f)<sup>62</sup>. During the following Pliocene lowstand (“Productive Series”<sup>52</sup>) the delta of the palaeo-Volga shifted 800 km to the south, while the endorheic Caspian lake shrank to  $\sim 25\%$  of its present-day size and was confined to the South Caspian Basin (Fig. 1).

The shorter Miocene Arabian hyperarid intervals correspond in a similar way to significant Ponto-Caspian lowstands at the end of the Meotian and Khersonian regional stages (6.25, 7.5, and 7.78 Ma) and during the Khersonian (8.75 Ma). The end-Bessarabian lowstand corresponds in our record to maximum DMAR values (Fig. 5e). During periods of pronounced Ponto-Caspian highstands (e.g., during the Akchagylia, Pontian, or Bessarabian) Mesopotamian climate is semi-arid to arid and Tigris runoff is high.

Our identification of the NADX agrees well with climate simulations for the early Pliocene (5–4 Ma), where zonal mean humidity indicates dryer-than-present midlatitudes in the northern hemisphere<sup>64</sup> (Fig. 2b, c), whereas late Pliocene models (3 Ma) reveal increased humidity in northern midlatitudes<sup>65</sup>. This suggests that in addition to a regional Paratethyan forcing, we may also interpret the NADX interval as a midlatitudinal response to tropical ocean forcing, in particular the Pacific in concert with the Indian Ocean. During the latest Miocene to early Pliocene (5.5–3.3 Ma), reduced zonal and meridional temperature gradients and a deep thermocline in the equatorial Pacific lead to sustained El Niño-like conditions (El Padre) with low amplitude El Niño–Southern Oscillation (ENSO) events<sup>66,67</sup>. During Pacific El Niño conditions, heating of the southwest Indian Ocean establishes the canonical Indian Ocean Dipole (IOD<sup>68</sup>) pattern, resulting in a strengthening of local Hadley circulation, stronger convergence, increased East African monsoon rain and substantial divergence anomalies over West Asia propagated by Rossby waves to the midlatitudes of Eurasia<sup>69</sup>. Starting from the mid-Piacenzian (after 3.3 Ma) increased amplitudes of ENSO events are observed, sometimes similar to extent values<sup>67</sup>, corresponding in our results to increased humidity and arid climate similar-to-present in Mesopotamia (Fig. 5g). In support of this teleconnection, an increase of winter precipitation with increasing ENSO amplitudes

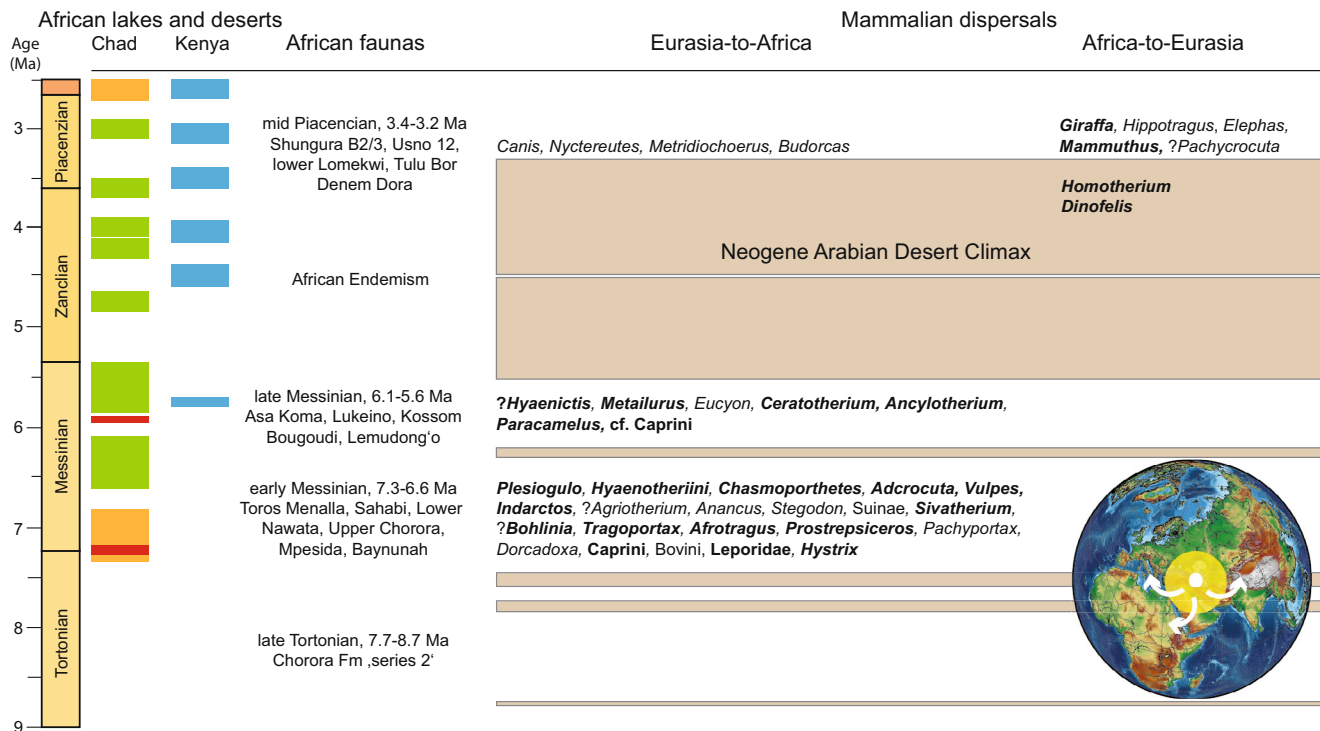


**Fig. 6 Intercontinental mammalian dispersals between Africa and Eurasia during the late Miocene and Pliocene and African lacustrine periods.** Mammalian taxa that most probably have dispersed into/from western (eastern) Eurasia are read in bold (regular). For discussion of fossil mammal taxonomy and biogeography see Supplementary information chapter 5. Dispersals of (semi-)aquatic mammals are excluded. Arabian hyperarid periods are highlighted in pale. Chronologic occurrences of deep lakes in Kenya (Omo-Turkana Basin<sup>71</sup>) are shown in blue and lacustrine facies as well as desert dunes in northern Chad<sup>73</sup> are marked in green, respectively red. Desertic periods in northern Sahara during Miocene<sup>56</sup> and western Sahara during Plio-Pleistocene<sup>74,76</sup> are shown in orange. The pictogram of a globe (created using generic mapping tools of ref. <sup>124</sup> and the topographic dataset ETOPO1 of ref. <sup>125</sup>) highlights the scale of desert expansion in West Asia, arrows symbolise dispersal routes during Miocene transient desertic events.

has been observed in present-day climatology of southwestern Iran<sup>70</sup>.

During the early Pliocene (with sustained equatorial El Padre-IOD conditions), the subtropics (10–30°N) behave opposite to midlatitudinal regions in showing positive zonal humidity relative to today<sup>64</sup>. Therefore, during the NADX interval, the rainfall gradient is expected to be maximal between East Africa and West Asia. This is corroborated by East African lake level history (Fig. 6), showing during the latest Miocene and Pliocene periodic development of deep lakes, paced by 400 kyr eccentricity maxima<sup>71</sup>, and the lack of long-term aridification<sup>72</sup>. Similarly, stratigraphic distribution of lake sediments in Chad show prevailing humid conditions in the Sahel between 6.5 and 3 Ma with recurrent lacustrine and peri-lacustrine facies (Fig. 6)<sup>73</sup> and persistent fluvial discharge off West Africa<sup>74</sup>. The oldest field evidence of a Sahara Desert<sup>54</sup> points to a first climax about 7.2 Ma<sup>55,56</sup>, in accord with the near absence of Mediterranean sapropels between 7.5 and 7.175 Ma<sup>75</sup>, followed by a desert event at 6 Ma<sup>73</sup>. Regular deserts start to develop in West Sahara from 2.7 to 2.5 Ma onward<sup>76</sup>. Thus, hyperarid periods in northern Arabia do not correspond to Sahara Desert expansions, suggesting out-of-phase relationships between tropical and extra-tropical aridity during the Neogene in the Old-World.

**Eurasian-African mammal interchange.** It has long been observed that faunal interchange between Eurasia and Africa was not reciprocal during the Neogene<sup>22</sup>, but strongly biased toward into-Africa dispersals during the late Miocene (Fig. 6 and see Supplementary information chapter 5 for detailed analysis). Stimulated by ideas of Charles Darwin<sup>77</sup> this pattern was explained

with the traffic-light model<sup>27</sup>, which assumes emerging land bridges during glacial times tracked by cool-adapted mammals southwards. During the Neogene however, eustatic sea-level fluctuations were neither as large as during the Pleistocene<sup>44</sup> (and hence did not open land bridges between Africa and Eurasia), nor were African immigrants cool-adapted, because their mid-latitudinal Eurasian source areas exhibit largely (sub-)tropical temperatures during the late Miocene<sup>78</sup>. Here, we propose that the Miocene imbalance between Eurasian and African transcontinental dispersers and the Pliocene African endemism (see ref. <sup>23</sup>, see below) can be largely explained by the out-of-phase relationship of desert formation in North Africa and North Arabia and the recurrent development of transient late Miocene and sustained Pliocene deserts in extra-tropical West Asia (Fig. 7).

To begin with, two isolated maxima of North Arabian desert expansions during late Tortonian (7.9–7.4 Ma, Fig. 5) triggered the most significant wave of Eurasian dispersers observed in Africa during the early Messinian (7.3–6.6 Ma), with first appearance of important tribes of carnivores, bovids, giraffids, suids, leporids, proboscidians, and possibly hominines. The majority of these immigrants inhabited savannah landscapes of the Pliocene biome in western Eurasia during late Tortonian times (e.g., *Adcrocuta*, *Ictitherium*, *Bohlinia*, *Tragoportax*, *Prostrepsiceros*; see Fig. 6), whereas others have eastern Eurasian affinities deriving from mesic habitats in South Asia (Siwaliks, e.g., *Stegodon*, *Suinae*, *Reduncini*, *Bovini*). A similar structured, but less species-rich wave of into-Africa dispersers can be observed during late Messinian (6.1–5.6 Ma), following the 6.25 Ma hyperarid event in North Arabia.

Next, in the wake of the Mediterranean desiccation at stage 2 of the MSC, the Arabian dispersal corridor turned into a durable



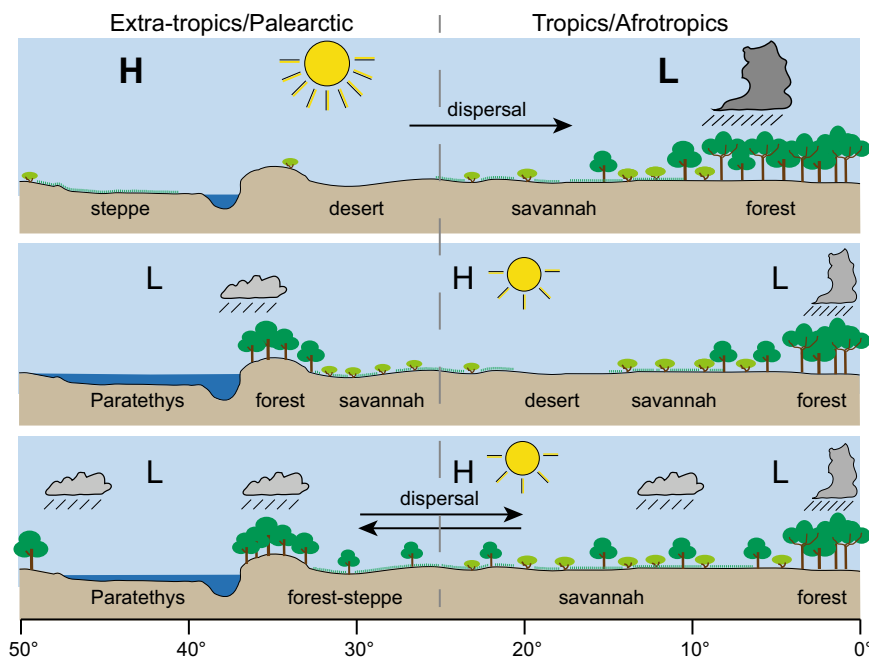


**Fig. 7** Idealized model explaining late Neogene mammalian dispersals between Palaeartic and Afrotropical biogeographic realms along a meridional transect between West Asia and East Africa (40°–55° E longitude). Upper panel: Reduced Paratethys and Arabian hyperaridity (e.g., at 6.25, 7.50, 7.78, 8.75 Ma) increase humidity gradient between subtropics and midlatitudes, thereby forcing Palaeartic savannah mammals (Pikermian biome) to disperse into Africa. Middle panel: Large Paratethys and North African aridity (e.g., at 7.2 and 6 Ma) increase humidity gradient between low-/mid-latitudes and subtropics preventing into-Africa dispersal. Lower panel: Large Paratethys and reduced African and Arabian aridity (absence of deserts) during mid-Piacenzian enables bi-directional dispersals between Palaeartic and Afrotropics (the usage of names for present-day biogeographic realms is conditionally to denote the territories, which through the Quaternary represent the respective units).

hyperarid barrier to terrestrial faunal interchange between Eurasia and Africa. Thus, in contrast to the transient late Miocene Arabian hyperaridity events, which did promote dispersals, the NADX (5.6–3.3 Ma) defined a long period during which Arabia served as vicariant agent. Indeed, many clades of African mammals, some of which already represented former Eurasian dispersers, diversified during the NADX through continental-scale African endemism, such as the Bovini (*Ugandax*, *Simatherium*), Alcephalini (*Damalacra*, *Parmularius*), Hippotragini (*Hippotragus*, *Oryx*), Reduncini (*Kobus*, *Redunca*), Sivatheriinae (*Sivatherium*), Tetraconodontinae (*Nyanzachoerus*, *Notochoerus*), Suinae (*Kolpochoerus*, *Potamochoerus*), Canidae (*Eucyon*), Hyaenidae (*Chasmodon*), Machairodontinae (*Homotherium*, *Dinofelis*), Dicerotini (*Ceratotherium*, *Diceros*), Elephantini (*Elephas*, *Mammuthus*, *Loxodonta*), and also Hominini (*Ardipithecus*, *Australopithecus*). In contrast, to our knowledge only two potential African immigrants into western Eurasia are documented between 4.0–3.6 Ma, the sabre-tooth cats *Dinofelis* and *Homotherium* (Fig. 6).

Finally, global warming and retreat of deserts during the mid-Piacenzian reactivated the Arabian corridor and enabled bi-directional faunal exchange between both landmasses, as evidenced by the spread of African taxa to Asia (*Elephas* and *Hippotragus*), Europe and the Levant (*Mammuthus* and *Giraffa*), and vice versa of groups of Eurasian mammals (e.g., true dogs, goats, warthogs) to Africa. These bi-directional dispersals continued further during the early Pleistocene. To conclude, the desert dynamics in West Asia had a strong control on large-scale mammalian dispersals between Africa and Eurasia. Our results are in support of models for the origin of the modern African savannah biome<sup>26</sup> by providing the driving forces for the late Miocene constitution, and the early Pliocene continental fragmentation of the Old-World Savannah Palaeobiome.

## Methods

**Age model and sampling.** A previous magnetostatigraphic study by Homke et al.<sup>28</sup> gives excellent temporal control for the 2.6 km thick sediment succession exposed in both structures using a best-fit solution correlating 22 normal polarity chrons or subchrons, which leads to absolute ages between 13 and 2 Ma. Nearly all magnetochrons present in this interval were identified by Homke et al.<sup>28</sup>, whose absolute ages were corrected here using the most recent geomagnetic polarity timescale<sup>79</sup>. In the present study, samples were taken from exactly the same georeferenced palaeomagnetic sampling sites of Homke et al.<sup>28</sup> using a handheld GPS device following exactly the investigated profiles. This procedure provided extremely high-resolution age-constraints for the studied samples with uncertainties related only to the exact position of the reversal between two consecutive points of opposite polarity in the order of  $\pm 50$  kyrs. Given limitations in the field at the Iran–Iraq border our primary strategy was to sample the 2.600 m thick profile evenly spaced to construct of geochemical and physical proxy data record. We achieved this goal with 84 sampled strata from silty horizons from the Zarrinabad and Changuleh profiles representing a mean (median) sampling resolution of 115 (90) kyrs.

**Proxy data record.** Each sample was analysed in terms of ionic composition, magnetic susceptibility, and grain-size distribution. In addition, as a reference for marine halite we measured eight samples from Phanerozoic rock salts.

Aqueous extracts (30–40 ml MilliQ water in 200–500 mg sample) from all samples were measured for cations ( $\text{Na}^+$ ,  $\text{K}^+$ ,  $\text{Ca}^{2+}$ ,  $\text{Mg}^{2+}$ ,  $\text{Sr}^{2+}$ ,  $\text{Ba}^{2+}$ ) and anions ( $\text{F}^-$ ,  $\text{Cl}^-$ ,  $\text{Br}^-$ ,  $\text{SO}_4^{2-}$ ,  $\text{NO}_3^-$ ,  $\text{PO}_4^{3-}$ ) by ion chromatography using a 930 Compact IC Flex chromatograph (Metrohm) in Tübingen (as described in ref.<sup>80</sup>). For a subset of the samples ( $n = 11$ ) each two aliquots were extracted to check for the importance of sample heterogeneity, which was found to be very minor. The major ions detected were  $\text{Na}^+$ ,  $\text{Cl}^-$ ,  $\text{Ca}^{2+}$ ,  $\text{SO}_4^{2-}$ , and  $\text{NO}_3^-$ , whereas  $\text{PO}_4^{3-}$  was practically absent, suggesting absence of anthropogenic or biogenic contamination (Supplementary Fig. S3 and Supplementary Data 1).

Magnetic bulk susceptibility was measured using an MFK-1 AGICO kappabridge housed in the Palaeomagnetic laboratory of University of Tübingen (Supplementary Fig. S2d).

Particle size distribution (PSD) was determined with a Laser Particle Sizer (Mastersizer 2000, Malvern Instruments, University of Tübingen) using sodium pyrophosphate ( $\text{Na}_4\text{P}_2\text{O}_7 \cdot 10 \text{H}_2\text{O}$ ) as dispersant. Pre-treatment of samples included decalcification<sup>55</sup>. End-member analysis of PSD along the profile was performed with EMMAgeo<sup>81</sup> to identify sedimentological distinct components and study their variation along the profile (see Supplementary information chapter 2,

Table S1, and Figs. S6–8 for details). The dust accumulation rate was calculated by multiplying the sedimentation rate with the relative contribution (score) of the fine-to-medium silt end member (2–30  $\mu\text{m}$ , with mode at 20  $\mu\text{m}$ ) and converted to dust mass accumulation rate by using a density of 2.65  $\text{g cm}^{-3}$ .

**Heavy mineral provenance.** For heavy mineral separation, we selected four fluvial sandstone samples (Gachsaran Fm, IZ 165 SS, 13.1 Ma; lower Agha Jari Fm, IZ 158 SS, 9.47 Ma; Lahbari Mb, IC 26c SS, 7.0 Ma and IC 67 SS, 4.27 Ma) in addition to four silty samples (lower Agha Jari Fm, IC 35, 6.25 Ma; Lahbari Mb, IC 45, 5.50 Ma, IC 50c, 4.93 Ma and IC 71, 3.98 Ma). Heavy minerals were separated from the crushed and sieved samples using sodiumheteropolytungstate in water at a density of 2.85  $\text{g cm}^{-3}$ , following the general separation scheme of Andó<sup>82</sup>. To avoid any biasing of ferromagnetic heavy minerals, no metal tools were used during the entire sample preparation process. Automated elemental analysis of single mineral grains was performed on a Quanta 600F scanning electron microscope (SEM) coupled to an Oxford x-max 80 EDX-detector. The SEM was operated at 25 kV in low-vacuum mode at 40 Pa and a spot size of 4  $\mu\text{m}$ , with a data acquisition time of 1 s per grain. Logging of morphometric parameters (length, width, shape) and elemental spectra was performed using the Oxford INCA software. Although heavy minerals were characterised in detail (see Supplementary information chapter 3 and Supplementary Data 3), single mineral types were grouped as opaque, mica, garnet, amphibole, pyroxene, epidote group, rutile, zircon, tourmaline, and other minerals to facilitate comparison with published data (see refs. 83–86 Supplementary Fig. S10). The “others” group comprises e.g., andalusite, apatite, barite, celestine, kyanite, monazite, olivine, sillimanite, titanite, etc. Individual grain size fractions with less than 200 transparent grains are generally interpreted with caution.

**Ponto-Caspian sea-level evolution.** The Eastern Parastethyan, resp. Ponto-Caspian sea-level curve (Fig. 5f) was modified according to refs. 51,62,87–89. The age of the Caspian lake-level drop and hence the base of the Productive Series<sup>90,91</sup> follows Van Baak et al.<sup>62</sup>. The end of the ‘Productive Series’ by a marine re-flooding of Caspian basin (Akchagylian transgression) is controversial. Ages vary between 3.6, 3.2, and 2.7 Ma<sup>52,88,92,93</sup>.

**The geochemistry of chloride and bromide.** As chloride and bromide tend to form highly soluble minerals, their ratio is not significantly affected by evapotranspiration<sup>94</sup>. The soil content of non-anthropogenic chloride and bromide originate from atmospheric dry and wet deposition or from evaporites leached by groundwater<sup>95,96</sup>. Atmospheric halogens stem from sea spray or from terrigenous mineral dust, especially in arid regions. Both sources can be distinguished by their characteristic chloride/bromide ratios. The  $\text{Cl}^-/\text{Br}^-$  molar ratio of seawater is 650<sup>97</sup>, similar to bulk deposition in near coastal areas<sup>94,96</sup>. In evaporitic settings this ratio stays constant until the halite stage is reached. As precipitated halite is generally bromide-poor,  $\text{Cl}^-/\text{Br}^-$  ratios in the residual brines strongly decrease, especially in some plays<sup>98,99</sup>. The first halite precipitating in marine evaporative stages has a  $\text{Cl}^-/\text{Br}^-$  molar ratio of around 20,000, which decrease significantly during later stages and in systems with several evaporates<sup>96,98,100</sup>. Furthermore, aged sea-salt and long-range transported dust can be depleted in chloride and especially bromide due to photochemical reactions and aerosol acidic components<sup>101</sup>.

In contrast, continental rainwater and dry deposition is commonly enriched in bromide relative to seawater due to particle-size dependent fractionation in aerosols and bromide release from vegetation and burned biomass<sup>102–104</sup>. There are also hints that plant material is enriched in bromide<sup>105,106</sup>. Decomposition of soil organic matter leads to a decrease of the  $\text{Cl}^-/\text{Br}^-$  ratio in vegetated soils, most pronounced in warm climates<sup>107,108</sup>.

We therefore expect that atmospheric deposition dominated by evaporites as halogen donors (e.g., desert dust) show  $\text{Cl}^-/\text{Br}^-$  molar ratios higher than 650. In contrast, wet or dry deposition by halogens of marine (as sea salt from Mediterranean >1000 km towards west) and/or biomass origins, but without significant evaporitic admixture from deserts, is expected to show  $\text{Cl}^-/\text{Br}^-$  molar ratios <650. The lowest  $\text{Cl}^-/\text{Br}^-$  molar ratios (<125, the mean ratio of upper tropospheric aerosols<sup>109</sup>) are expected to occur in our record in soil samples reflecting highest past biomass, respectively palaeo-humidity. Leaching of pure marine halite deposits will show high molar  $\text{Cl}^-/\text{Br}^-$  ratios much over 3500<sup>96</sup>, which are not observed in our record.

**Atmospheric nitrate.** Atmospheric nitrate (as nitric acid) is formed by photochemical reactions of NOx and ozone on aerosol surfaces<sup>110,111</sup>. Atmospheric chloride derives from sea spray and terrigenous (evaporitic) dust<sup>112,113</sup>. In aged sea-salt particles (e.g., far from the sea) chloride (and bromide) can be partly or entirely substituted by nitrate<sup>101,110,111,113</sup>. This results in significant enrichment of nitrate in atmospheric deposition relative to chloride. The chloride/nitrate molar ratios from oceanic deep waters are in the range of 11–14  $\times 10^3$  (Supplementary Fig. S4 and Supplementary Data 2). Our data for halite from marine evaporites ( $n = 8$ ; Permian, Triassic, Miocene, Recent) also indicate very high chloride/nitrate molar ratios up to 53  $\times 10^3$  (Supplementary Fig. S4 and Supplementary Data 2). A literature survey on chloride and nitrate concentrations from mid-latitude hyperarid desert soils (Atacama, Mojave, Death Valley, Turpan Hami, Negev;

$n = 193$ ) reveal however, that chloride/nitrate molar ratios do not exceed 700 (median value 12.3; Supplementary Fig. S4 and Supplementary Data 2) similar to our results from the Agha Jari Fm ( $n = 80$ , median value 14.0; Fig. 5d and Supplementary Data 1), except sample IC45. Here, the ratio is 12.77  $\times 10^3$  (Fig. 5d and Supplementary Data 1), suggesting a marine origin of anions from this sample dated by magnetostratigraphic correlation to 5.50  $\pm$  0.05 Ma.

**Climatic interpretation of nitrate and chloride content of soils.** Following Ewing et al.<sup>36</sup> the content of soluble salts in desert soils reveal thresholds along a humidity gradient from hyperarid to arid conditions, with most soluble salts preserved in dryer soils. In particular chloride and nitrate contents in soils are excellent proxies for hyperaridity<sup>36,111,114–116</sup>. Due to the absence of leaching, both highly soluble anions accumulate in hyper-arid regions (precipitation to potential evapotranspiration, P/PET < 0.05) from atmospheric wet and dry deposition<sup>88,117</sup>. To discriminate between hyperarid (P/PET < 0.05), arid (P/PET 0.05–0.2), and semi-arid (P/PET > 0.2) climates in Mesopotamia we adopt empirical relationships between aridity and chloride/nitrate concentrations established in major mid-latitude deserts.

Ewing et al.<sup>36</sup> investigated soluble salt contents in Atacama Desert along a humidity gradient within hyperarid conditions, ranging in P/PET from 0.005 to 0.05. Chloride (nitrate) concentrations vary between 12,000 (500) and 40 (2)  $\mu\text{mol g}^{-1}$ , the lowest values are approached at the hyperarid to arid transition. In the arid (P/PET 0.07) Negev Desert, Rosenthal et al.<sup>37</sup> find maximum chloride (nitrate) concentrations of 10 (0.5)  $\mu\text{mol g}^{-1}$ , comparable to the arid (P/PET 0.14) Mu Us Desert, where Jin et al.<sup>118</sup> find maximum nitrate concentrations at 0.07  $\mu\text{mol g}^{-1}$ . Similar values have been found in other major mid-latitude deserts<sup>37,115,118–120</sup>. Based on these findings we set the chloride (nitrate) thresholds for the hyperarid-to-arid transition at 40 (2)  $\mu\text{mol g}^{-1}$  and for the arid-to-semi-arid transition at 0.2 (0.05)  $\mu\text{mol g}^{-1}$  (Table 1). However, we have to admit that soluble salt concentration may vary between deserts due to local control on salt preservation and (mostly unknown in details) palaeoclimatic conditions<sup>121</sup>, so that the absolute values of our thresholds have to be seen as approximations.

Nonetheless, comparing our palaeoclimatic interpretations based on chloride and nitrate thresholds with measured  $\text{Cl}^-/\text{Br}^-$  molar ratios finds a generally good correspondence with theoretically expected values (Supplementary Fig. S5). The  $\text{Cl}^-/\text{Br}^-$  molar ratios of samples interpreted as hyperarid reach values well above seawater (650), suggesting that their halogens derive predominantly from desert dust. In contrast, arid samples are enriched in bromine relative to seawater, which is even more amplified in samples interpreted to derive from semi-arid climates, which fall generally below upper tropospheric  $\text{Cl}^-/\text{Br}^-$  ratios, probably due to bromide enrichment by biomass.

**Palynology.** Around 20 g of the sample IC44b (the oldest sample of our NADX interval) was prepared for palynological analysis following standard extraction techniques including HCl-HF demineralization treatment<sup>122</sup>. Afterwards, the residues were sieved using 10  $\mu\text{m}$  nylon meshes. No oxidative acids were employed. An aliquot of the concentrate residue of each sample was mounted on coverslips dried at 30–40 °C to get a single plane of focus, and adhered to the coverslip using Glycerine Gelatine. Semi-quantitative and qualitative analyses have been done. Counts of 150 palynomorphs were made through several traverses per each slide. A selected suite of the well-preserved pollen taxa was photographed and illustrated (Supplementary Fig. S11). Microscopic investigation and photomicrographs were made using Axiocam 512 color camera attached to a Zeiss Axio Imager.M2 microscope.

**Mammalian dispersals between Africa and Eurasia.** To investigate the late Neogene history of mammalian megafaunal dispersals we reviewed existing literature on African and Eurasian fossil mammals between 9 and 3 Ma, including their stratigraphic or chronologic ages (see Supplementary information chapter 5 for details).

## Code availability

All data generated or analysed during this study are included in this published Article (and its Supplementary Information and Supplementary Data 1–3, deposited at <https://doi.org/10.5281/zenodo.4704789>).

Received: 21 July 2020; Accepted: 24 March 2021;

Published online: 18 May 2021

## References

- Prospero, J. M., Ginoux, P., Torres, O., Nicholson, S. E. & Gill, T. E. Environmental characterization of global sources of atmospheric soil dust identified with the Nimbus 7 Total Ozone Mapping Spectrometer (TOMS) absorbing aerosol product. *Rev. Geophys.* **40**, 2-1–2-31 (2002).
- Prospero, J. M. & Lamb, P. J. African droughts and dust transport to the Caribbean: climate change implications. *Science* **302**, 1024–1027 (2003).

3. Jickells, T. et al. Global iron connections between desert dust, ocean biogeochemistry, and climate. *science* **308**, 67–71 (2005).
4. Mahowald, N. M. et al. Atmospheric global dust cycle and iron inputs to the ocean. *Glob. Biogeochem. Cycles* **19**, <https://doi.org/10.1029/2004GB002402> (2005).
5. Bristow, C. S., Hudson-Edwards, K. A. & Chappell, A. Fertilizing the Amazon and equatorial Atlantic with West African dust. *Geophys. Res. Lett.* **37**, <https://doi.org/10.1029/2010GL043486> (2010).
6. Rizzolo, J. A. et al. Soluble iron nutrients in Saharan dust over the central Amazon rainforest. *Atmos. Chem. Phys.* **17**, 2673–2687 (2017).
7. Micheels, A., Eronen, J. & Mosbrugger, V. The Late Miocene climate response to a modern Sahara desert. *Glob. Planet. Change* **67**, 193–204 (2009).
8. Lohmann, G., Butzin, M. & Bickert, T. Effect of vegetation on the Late Miocene ocean circulation. *J. Mar. Sci. Eng.* **3**, 1311–1333 (2015).
9. Vinoj, V. et al. Short-term modulation of Indian summer monsoon rainfall by West Asian dust. *Nat. Geosci.* **7**, 308–313 (2014).
10. Dave, P., Bhushan, M. & Venkataraman, C. Aerosols cause intraseasonal short-term suppression of Indian monsoon rainfall. *Sci. Rep.* **7**, 1–12 (2017).
11. Besnard, G., de Casas, R., Christin, R. & Vargas, P.-A. P. Phylogenetics of Olea (Oleaceae) based on plastid and nuclear ribosomal DNA sequences: tertiary climatic shifts and lineage differentiation times. *Ann. Bot.* **104**, 143–160 (2009).
12. Désamoré, A. et al. Out of Africa: north-westwards Pleistocene expansions of the heather *Erica arborea*. *J. Biogeogr.* **38**, 164–176 (2011).
13. Denk, T., Güner, H. T. & Grimm, G. W. From mesic to arid: Leaf epidermal features suggest preadaptation in Miocene dragon trees (*Dracaena*). *Rev. Palaeobot. Palynol.* **200**, 211–228 (2014).
14. Mairal, M., Pokorný, L., Aldasoro, J. J., Alarcón, M. & Sanmartín, I. Ancient vicariance and climate-driven extinction explain continental-wide disjunctions in Africa: the case of the Rand Flora genus *Canarina* (Campanulaceae). *Mol. Ecol.* **24**, 1335–1354 (2015).
15. Douady, C. J. et al. The Sahara as a vicariant agent, and the role of Miocene climatic events, in the diversification of the mammalian order Macroscelidea (elephant shrews). *Proc. Natl Acad. Sci.* **100**, 8325–8330 (2003).
16. Carranza, S., Arnold, E., Geniez, P., Roca, J. & Mateo, J. Radiation, multiple dispersal and parallelism in the skinks, Chalcides and Sphenops (Squamata: Scincidae), with comments on Scincus and Scincopus and the age of the Sahara Desert. *Mol. Phylogenet. Evol.* **46**, 1071–1094 (2008).
17. Brito, J. C. et al. Unravelling biodiversity, evolution and threats to conservation in the Sahara-Sahel. *Biol. Rev.* **89**, 215–231 (2014).
18. Gonçalves, D. V. et al. The role of climatic cycles and trans-Saharan migration corridors in species diversification: biogeography of *Psammophis schokari* group in North Africa. *Mol. Phylogenet. Evol.* **118**, 64–74 (2018).
19. Lado, S., Alves, P. C., Islam, M. Z., Brito, J. C. & Melo-Ferreira, J. The evolutionary history of the Cape hare (*Lepus capensis sensu lato*): insights for systematics and biogeography. *Heredity* **123**, 634–646 (2019).
20. Moutinho, A. F. et al. Evolutionary history of two cryptic species of northern African jerboas. *BMC Evol. Biol.* **20**, 1–16 (2020).
21. Solounias, N., Plavcan, J., Quade, J. & Witmer, L. in *The Evolution of Neogene Terrestrial Ecosystems in Europe* (eds Rook, L. et al.) Ch. 22, 436–453 (Cambridge University Press, 1999).
22. Thomas, H. Les bovidae (Artiodactyla: Mammalia) du miocene du sous-continent indien, de la péninsule arabique et de l'Afrique: Biostatigraphie, biogéographie et ecologie. *Palaeogeogr. Palaeoclimatol. Palaeoecol.* **45**, 251–299 (1984).
23. Bibi, F. Mio-Pliocene faunal exchanges and African biogeography: the record of fossil bovids. *PLoS ONE* **6**, e16688 (2011).
24. Bibi, F. A multi-calibrated mitochondrial phylogeny of extant Bovidae (Artiodactyla, Ruminantia) and the importance of the fossil record to systematics. *BMC Evol. Biol.* **13**, 166 (2013).
25. Begun, D. R., Nargolwalla, M. C. & Kordos, L. European Miocene hominids and the origin of the African ape and human clade. *Evol. Anthropol.* **21**, 10–23 (2012).
26. Kaya, F. et al. The rise and fall of the Old World savannah fauna and the origins of the African savannah biome. *Nat. Ecol. Evol.* **2**, 241–246 (2018).
27. Vrba, E. S. On the connections between paleoclimate and evolution. In *Paleoclimate and evolution, with emphasis on human origins*. (eds Vrba, E. S., Denton, G. H., Partridge, T. C. & Burckle, L. H.) p. 24–45 (Yale University Press, New Haven and London, 1995).
28. Homke, S., Vergés, J., Garcés, M., Emami, H. & Karpuz, R. Magnetostratigraphy of Miocene–Pliocene Zagros foreland deposits in the front of the Push-e Kush arc (Lurestan Province, Iran). *Earth Planet. Sci. Lett.* **225**, 397–410 (2004).
29. Alavi, M. Tectonics of the Zagros orogenic belt of Iran: new data and interpretations. *Tectonophysics* **229**, 211–238 (1994).
30. Berberian, M. Master “blind” thrust faults hidden under the Zagros folds: active basement tectonics and surface morphotectonics. *Tectonophysics* **241**, 193–224 (1995).
31. Mather, A., Stokes, M., Pirrie, D. & Hartley, R. Generation, transport and preservation of armoured mudballs in an ephemeral gully system. *Geomorphology* **100**, 104–119 (2008).
32. Bachmann, G. H. & Wang, Y. Armoured mud balls as a result of ephemeral fluvial flood in a humid climate: modern example from Guizhou Province, South China. *J. Palaeogeogr.* **3**, 410–418 (2014).
33. Vicente, A., Expósito, M., Sanjuan, J. & Martín-Closas, C. Small sized charophyte gyrogonites in the Maastrichtian of Coll de Nargó, Eastern Pyrenees: an adaptation to temporary floodplain ponds. *Cretac. Research* **57**, 443–456 (2016).
34. Fakhari, M. D., Axen, G. J., Horton, B. K., Hassanzadeh, J. & Amini, A. Revised age of proximal deposits in the Zagros foreland basin and implications for Cenozoic evolution of the High Zagros. *Tectonophysics* **451**, 170–185 (2008).
35. Emami, H. et al. Structure of the Mountain Front Flexure along the Anaran anticline in the Pusht-e Kuh Arc (NW Zagros, Iran): insights from sand box models. *Geol. Soc. Lond. Spec. Publ.* **330**, 155–178 (2010).
36. Ewing, S. A. et al. A threshold in soil formation at Earth’s arid–hyperarid transition. *Geochim. Cosmochim. Acta* **70**, 5293–5322 (2006).
37. Rosenthal, E., Magaritz, M., Ronen, D. & Roded, R. Origin of nitrates in the Negev Desert, Israel. *Appl. Geochem.* **2**, 347–354 (1987).
38. Michalski, G., Böhlke, J. & Thiemens, M. Long term atmospheric deposition as the source of nitrate and other salts in the Atacama Desert, Chile: new evidence from mass-independent oxygen isotopic compositions. *Geochim. Cosmochim. Acta* **68**, 4023–4038 (2004).
39. Mouthereau, F., Lacombe, O. & Vergés, J. Building the Zagros collisional orogen: timing, strain distribution and the dynamics of Arabia/Eurasia plate convergence. *Tectonophysics* **532**, 27–60 (2012).
40. Reynolds, R. L. et al. Dust emission from wet and dry playas in the Mojave Desert, USA. *Earth Surf. Process. Landf.* **32**, 1811–1827 (2007).
41. Cosentino, D. et al. Refining the Mediterranean “Messinian gap” with high-precision U–Pb zircon geochronology, central and northern Italy. *Geology* **41**, 323–326 (2013).
42. Lisiecki, L. E. & Raymo, M. E. A Pliocene–Pleistocene stack of 57 globally distributed benthic  $\delta^{18}O$  records. *Paleoceanography* **20**, <https://doi.org/10.1029/2004PA001071> (2005).
43. Tan, N. et al. Exploring the MIS M2 glaciation occurring during a warm and high atmospheric CO<sub>2</sub> Pliocene background climate. *Earth Planet. Sci. Lett.* **472**, 266–276 (2017).
44. Miller, K. G. et al. High tide of the warm Pliocene: Implications of global sea level for Antarctic deglaciation. *Geology* **40**, 407–410 (2012).
45. Ohneiser, C. et al. Antarctic glacio-eustatic contributions to late Miocene Mediterranean desiccation and reflooding. *Nat. Commun.* **6**, 1–10 (2015).
46. Haywood, A. M., Dowsett, H. J. & Dolan, A. M. Integrating geological archives and climate models for the mid-Pliocene warm period. *Nat. Commun.* **7**, 1–14 (2016).
47. Manzi, V. et al. Age refinement of the Messinian salinity crisis onset in the Mediterranean. *Terra Nova* **25**, 315–322 (2013).
48. Ryan, W. B. Decoding the Mediterranean salinity crisis. *Sedimentology* **56**, 95–136 (2009).
49. Roveri, M. et al. The Messinian Salinity Crisis: past and future of a great challenge for marine sciences. *Mar. Geol.* **352**, 25–58 (2014).
50. Madof, A. S., Bertoni, C. & Lofi, J. Discovery of vast fluvial deposits provides evidence for drawdown during the late Miocene Messinian salinity crisis. *Geology* **47**, 171–174 (2019).
51. Krijgsman, W., Stoica, M., Vasiliev, I. & Popov, V. Rise and fall of the Paratethys Sea during the Messinian Salinity Crisis. *Earth Planet. Sci. Lett.* **290**, 183–191 (2010).
52. van Baak, C. G. et al. Paratethys response to the Messinian salinity crisis. *Earth Sci. Rev.* **172**, 193–223 (2017).
53. Böhme, M., Ilg, A. & Winkhofer, M. Late Miocene “washhouse” climate in Europe. *Earth Planet. Sci. Lett.* **275**, 393–401 (2008).
54. Schuster, M. et al. The age of the Sahara desert. *Science* **311**, 821–821 (2006).
55. Böhme, M. et al. Messinian age and savannah environment of the possible hominin *Graecopithecus* from Europe. *PLoS ONE* **12**, e0177347 (2017).
56. Böhme, M., Van Baak, C. G., Prieto, J., Winkhofer, M. & Spassov, N. Late Miocene stratigraphy, palaeoclimate and evolution of the Sandanski Basin (Bulgaria) and the chronology of the Pliocene faunal changes. *Glob. Planet. Change* **170**, 1–19 (2018).
57. Aljani, B. & Garman, J. R. Synoptic climatology of precipitation in Iran. *Ann. Assoc. Am. Geogr.* **75**, 404–416 (1985).
58. Perşoiu, A., Ionita, M. & Weiss, H. Atmospheric blocking induced by the strengthened Siberian High led to drying in west Asia during the 4.2 ka BP event—a hypothesis. *Clim. Past* **15**, 781–793 (2019).
59. Ramstein, G., Fluteau, F., Besse, J. & Joussaume, S. Effect of orogeny, plate motion and land–sea distribution on Eurasian climate change over the past 30 million years. *Nature* **386**, 788–795 (1997).

60. Zhongshi, Z., Wang, H., Guo, Z. & Jiang, D. What triggers the transition of palaeoenvironmental patterns in China, the Tibetan Plateau uplift or the Paratethys Sea retreat? *Palaeogeogr. Palaeoclimatol. Palaeoecol.* **245**, 317–331 (2007).
61. Najafi, M. S., Sarraf, B., Zarrin, A. & Rasouli, A. Climatology of atmospheric circulation patterns of Arabian dust in western Iran. *Environ. Monit. Assess.* **189**, 473 (2017).
62. van Baak, C. G., Stoica, M., Grothe, A., Aliyeva, E. & Krijgsman, W. Mediterranean-Paratethys connectivity during the Messinian salinity crisis: the Pontian of Azerbaijan. *Glob. Planet. Change* **141**, 63–81 (2016).
63. Naidina, O. D. & Richards, K. The Akchagyl stage (late Pliocene-early Pleistocene) in the North Caspian region: Pollen evidence for vegetation and climate change in the Urals-Emba region. *Quat. Int.* **540**, 22–37 (2020).
64. Burls, N. J. & Fedorov, A. V. Wetter subtropics in a warmer world: contrasting past and future hydrological cycles. *Proc. Natl Acad. Sci.* **114**, 12888–12893 (2017).
65. Colleon, F., Cherchi, A., Masina, S. & Brierley, C. M. Impact of global SST gradients on the Mediterranean runoff changes across the Plio-Pleistocene transition. *Paleoceanography* **30**, 751–767 (2015).
66. Holbourn, A. E. et al. Late Miocene climate cooling and intensification of southeast Asian winter monsoon. *Nat. Commun.* **9**, 1–13 (2018).
67. White, S. & Ravelo, A. Dampened El Niño in the early Pliocene warm period. *Geophys. Res. Lett.* **47**, e2019GL085504 (2020).
68. Tozuka, T., Endo, S. & Yamagata, T. Anomalous Walker circulations associated with two flavors of the Indian Ocean Dipole. *Geophys. Res. Lett.* **43**, 5378–5384 (2016).
69. Annamalai, H., Okajima, H. & Watanabe, M. Possible impact of the Indian Ocean SST on the Northern Hemisphere circulation during El Niño. *J. Clim.* **20**, 3164–3189 (2007).
70. Nazemosadat, M., Samani, N., Barry, D. & Molaii Niko, M. ENSO forcing on climate change in Iran: precipitation analysis. *Iran. J. Sci. Technol. Trans. B* **30**, 555–565 (2006).
71. Trauth, M. H. et al. High- and low-latitude forcing of Plio-Pleistocene East African climate and human evolution. *J. Hum. Evol.* **53**, 475–486 (2007).
72. Blumenthal, S. A. et al. Aridity and hominin environments. *Proc. Natl Acad. Sci.* **114**, 7331–7336 (2017).
73. Lebatard, A.-E. et al. Application of the authigenic  $^{10}\text{Be}/^{9}\text{Be}$  dating method to continental sediments: reconstruction of the Mio-Pleistocene sedimentary sequence in the early hominid fossiliferous areas of the northern Chad Basin. *Earth Planet. Sci. Lett.* **297**, 57–70 (2010).
74. Tiedemann, R., et al. Proc. ODP, Sci. Results. 241–277.
75. Hilgen, F. et al. Integrated stratigraphy and astrochronology of the Messinian GSSP at Oued Akrech (Atlantic Morocco). *Earth Planet. Sci. Lett.* **182**, 237–251 (2000).
76. Dupont, L. M. & Leroy, S. A. *Steps Toward Drier Climatic Conditions in Northwestern Africa during the Upper Pliocene. Paleoclimate and Evolution with Emphasis on Human Origins* 289–298 (Yale University Press, 1995)
77. Darwin, C. & Bynum, W. F. *The Origin of Species by Means of Natural Selection: Or, the Preservation of favored Races in the Struggle for Life* (Penguin Harmondsworth, 2009).
78. Herbert, T. D. et al. Late Miocene global cooling and the rise of modern ecosystems. *Nat. Geosci.* **9**, 843–847 (2016).
79. Gradstein, F. M., Ogg, J. G., Schmitz, M. B. & Ogg, G. M. *The Geologic Time Scale 2012*. (Elsevier, 2012).
80. Epp, T. et al. Vegetation canopy effects on total and dissolved Cl, Br, F and I concentrations in soil and their fate along the hydrological flow path. *Sci. Total Environ.* **712**, 135473 (2020).
81. Dietze, E. & Dietze, M. Grain-size distribution unmixing using the R package EMMAgeo. *E&G-Quat. Sci. J.* **68**, 29–46 (2019).
82. Andò, S. Gravimetric separation of heavy minerals in sediments and rocks. *Minerals* **10**, 273 (2020).
83. Al-Juboury, A. I. & Al-Miarmy, F. A. Geochemical variations in heavy minerals as provenance indications: application to the Tigris river sand, northern Iraq. *J. Mediter. Earth Sci.* **1**, 33–45 (2009).
84. Garzanti, E. et al. The Euphrates-Tigris-Karun river system: Provenance, recycling and dispersal of quartz-poor foreland-basin sediments in arid climate. *Earth Sci. Rev.* **162**, 107–128 (2016).
85. Philip, G. Mineralogy of the Recent sediments of Tigris and Euphrates rivers and some of the older detrital deposits. *J. Sediment. Res.* **38**, 35–44 (1968).
86. Škoček, V. & Saadallah, A. Grain-size distribution, carbonate content and heavy minerals in eolian sands, southern desert, Iraq. *Sediment. Geol.* **8**, 29–46 (1972).
87. Popov, S., Antipov, M., Zastrozhnov, A., Kurina, E. & Pinchuk, T. Sea-level fluctuations on the northern shelf of the Eastern Paratethys in the Oligocene-Neogene. *Stratigr. Geol. Correl.* **18**, 200–224 (2010).
88. Krijgsman, W. et al. Quaternary time scales for the Pontocaspian domain: interbasinal connectivity and faunal evolution. *Earth Sci. Rev.* **188**, 1–40 (2019).
89. van Baak, C. G. et al. Messinian events in the Black Sea. *Terra Nova* **27**, 433–441 (2015).
90. Green, T., Abdullayev, N., Hossack, J., Riley, G. & Roberts, A. M. *Sedimentation and Subsidence in the South Caspian Basin, Azerbaijan* vol. 312 (Geological Society, London, Special Publications, 2009) 241–260 (2009).
91. Abdullayev, N. R., Riley, G. W. & Bowman, A. P. Regional controls on lacustrine sandstone reservoirs: the Pliocene of the South Caspian Basin. (2012).
92. Trubikhin, V. Paleomagnetic data for the Pontian. *Chronostratigraphie und Neostatotypen-Pontien. Chronostratigraphie und Neostatotypen, Zagreb-Beograd.* 76–79 (1989).
93. Van Baak, C. G. et al. A magnetostratigraphic time frame for Plio-Pleistocene transgressions in the South Caspian Basin, Azerbaijan. *Glob. Planet. Change* **103**, 119–134 (2013).
94. Davis, S. N., Fabryka-Martin, J. T. & Wolfsberg, L. E. Variations of bromide in potable ground water in the United States. *Ground Water* **42**, 902–909 (2004).
95. Davis, S. N., Whittemore, D. O. & Fabryka-Martin, J. Uses of chloride/bromide ratios in studies of potable water. *Ground Water* **36**, 338–350 (1998).
96. Alcalá, F. J. & Custodio, E. Using the Cl/Br ratio as a tracer to identify the origin of salinity in Spain and Portugal. *J. Hydrol.* **359**, 189–207 (2008).
97. Dickson, A. & Goyet, C. *Handbook of Methods for the Analysis of the Various Parameters of the Carbon Dioxide System in Sea Water* 166–187 (ORNL/CDIAC-74, U. S. Department of Energy, 1994).
98. Tan, H., Ma, H., Li, B., Zhang, X. & Xiao, Y. Strontium and boron isotopic constraint on the marine origin of the Khammuane potash deposits in southeastern Laos. *Chin. Sci. Bull.* **55**, 3181–3188 (2010).
99. Turk, L., Davis, S. & Bingham, C. Hydrogeology of lacustrine sediments, Bonneville Salt Flats, Utah. *Econ. Geol.* **68**, 65–78 (1973).
100. Sun, S. et al. Bromine content and Br/Cl molar ratio of halite in a core from Laos: implications for origin and environmental changes. *Carbon. Evaporites* **34**, 1107–1115 (2019).
101. Fomba, K. W. et al. Long-term chemical characterization of tropical and marine aerosols at the CVAO: field studies (2007 to 2011). *Atmos. Chem. Phys.* **14**, 3917–3971 (2014).
102. Manó, S. & Andreae, M. O. Emission of methyl bromide from biomass burning. *Science* **263**, 1255–1257 (1994).
103. Goni, I., Fellman, E. & Edmunds, W. Rainfall geochemistry in the Sahel region of northern Nigeria. *Atmos. Environ.* **35**, 4331–4339 (2001).
104. Horst, A. et al. Stable bromine isotopic composition of methyl bromide released from plant matter. *Geochim. Cosmochim. Acta* **125**, 186–195 (2014).
105. Helder, R. The absorption of labelled chloride and bromide ions by young intact barley plants. *Acta Bot. Neerl.* **13**, 488–506 (1965).
106. Bowen, H. J. M. *Environmental Chemistry of the Elements* (Academic Press, 1979).
107. Gerritse, R. G. & George, R. J. The role of soil organic matter in the geochemical cycling of chloride and bromide. *J. Hydrol.* **101**, 83–95 (1988).
108. Wishkerman, A. et al. Abiotic methyl bromide formation from vegetation, and its strong dependence on temperature. *Environ. Sci. Technol.* **42**, 6837–6842 (2008).
109. Delany, A. C., Pollock, W. H. & Shedlovsky, J. P. Tropospheric aerosol—relative contribution of marine and continental components. *J. Geophys. Res.* **78**, 6249–6265 (1973).
110. Pérez-Fodich, A. et al. Climate change and tectonic uplift triggered the formation of the Atacama Desert's giant nitrate deposits. *Geology* **42**, 251–254 (2014).
111. Reich, M. & Bao, H. M. Nitrate deposits of the Atacama Desert: a marker of long-term hyperaridity. *Elements* **14**, 251–256 (2018).
112. Erickson, D. J. III & Duce, R. A. On the global flux of atmospheric sea salt. *J. Geophys. Res.* **93**, 14079–14088 (1988).
113. Murphy, D. M. et al. The distribution of sea-salt aerosol in the global troposphere. *Atmos. Chem. Phys.* **19**, <https://doi.org/10.5194/acp-19-4093-2019> (2019).
114. Walvoord, M. A. et al. A reservoir of nitrate beneath desert soils. *Science* **302**, 1021–1024 (2003).
115. Graham, R. C., Hirmas, D. R., Wood, Y. A. & Amrhein, C. Large near-surface nitrate pools in soils capped by desert pavement in the Mojave Desert, California. *Geology* **36**, 259–262 (2008).
116. Voigt, C., Klipsch, S., Herwartz, D., Chong, G. & Staubwasser, M. The spatial distribution of soluble salts in the surface soil of the Atacama Desert and their relationship to hyperaridity. *Glob. Planet. Change* **184**, 103077 (2020).
117. Böhlke, J., Ericksen, G. & Revesz, K. Stable isotope evidence for an atmospheric origin of desert nitrate deposits in northern Chile and southern California, USA. *Chem. Geol.* **136**, 135–152 (1997).
118. Jin, Z., Zhu, Y., Li, X., Dong, Y. & An, Z. Soil N retention and nitrate leaching in three types of dunes in the Mu Us desert of China. *Sci. Rep.* **5**, 14222 (2015).

119. Ericksen, G. E., Hosterman, J. W. & Amand, P. S. Chemistry, mineralogy and origin of the clay-hill nitrate deposits, Amargosa River valley, Death Valley region, California, USA. *Chem. Geol.* **67**, 85–102 (1988).
120. Qin, Y. et al. Massive atmospheric nitrate accumulation in a continental interior desert, northwestern China. *Geology* **40**, 623–626 (2012).
121. Lybrand, R. A. et al. Nitrate, perchlorate, and iodate co-occur in coastal and inland deserts on Earth. *Chemical Geology* **442**, 174–186 (2016).
122. Wood, G. in *American Association of Stratigraphic Palynologists Foundation* vol. 1 29–50 (1996).
123. Wallace, A. *The Geographical Distribution of Animals* Vol. I & II (Harper and Brothers, 1876).
124. Wessel, P. & Luis, J. F. The GMT/MATLAB Toolbox. *Geochem. Geophys. Geosyst.* **18**, 811–823 (2017).
125. Amante, C. & Eakins, B. *ETOPO1 Global Relief Model Converted to PanMap Layer Format* (NOAA-National Geophysical Data Center, 2009).
126. Flint, A. L., Flint, L. E., Curtis, J. A. & Buesch, D. C. A preliminary water balance model for the Tigris and Euphrates river system. US Geological Survey, Water Budget Report (2011).

## Acknowledgements

The authors thank Denis Geraads (CNRS and MNHN, Paris) for very valuable discussions on African mammal taxonomy and Christoph Hartkopf-Fröder (Geological Survey of North Rhine-Westphalia, Krefeld) for running the palynological processing at his lab. We are furthermore grateful for technical support to Agnes Fatz and Gabriele Stoschek (Senckenberg Centre for Human Evolution and Palaeoenvironment and University of Tübingen) and to Shirin Zarei and Mostafa Aseh (both Geologic Survey of Iran) for assistance during fieldwork. The manuscript benefits from three anonymous reviewers. H.E. acknowledges financial support by Alexander von Humboldt Foundation, Germany (EGY—1190326—GF-P).

## Author contributions

M.B. designed the study; M.B., N.S., M.R.M., A.G., U.K., M.M., C.D., G.U., H.E., D.R.B., and M.W. collected the data and performed the analyses; M.B., N.S., and M.W. discussed the results and wrote the paper.

## Funding

Open Access funding enabled and organized by Projekt DEAL.

## Competing interests

The authors declare no competing interests.

## Additional information

**Supplementary information** The online version contains supplementary material available at <https://doi.org/10.1038/s43247-021-00158-y>.

**Correspondence** and requests for materials should be addressed to M.Böh.

**Peer review information** Primary handling editor: Joe Aslin.

**Reprints and permission information** is available at <http://www.nature.com/reprints>

**Publisher's note** Springer Nature remains neutral with regard to jurisdictional claims in published maps and institutional affiliations.



**Open Access** This article is licensed under a Creative Commons Attribution 4.0 International License, which permits use, sharing, adaptation, distribution and reproduction in any medium or format, as long as you give appropriate credit to the original author(s) and the source, provide a link to the Creative Commons license, and indicate if changes were made. The images or other third party material in this article are included in the article's Creative Commons license, unless indicated otherwise in a credit line to the material. If material is not included in the article's Creative Commons license and your intended use is not permitted by statutory regulation or exceeds the permitted use, you will need to obtain permission directly from the copyright holder. To view a copy of this license, visit <http://creativecommons.org/licenses/by/4.0/>.

© The Author(s) 2021